

NIHAO project I: Reproducing the inefficiency of galaxy formation across cosmic time with a large sample of cosmological hydrodynamical simulations.

Liang Wang^{1,2,3*}, Aaron A. Dutton², Gregory S. Stinson², Andrea V. Macciò²,
Camilla Penzo¹, Xi Kang,¹ Ben W. Keller⁴, James Wadsley⁴

¹Purple Mountain Observatory, the Partner Group of MPI für Astronomie, 2 West Beijing Road, Nanjing 210008, China

²Max-Planck-Institut für Astronomie, Königstuhl 17, 69117 Heidelberg, Germany

³University of Chinese Academy of Science, 19A Yuquan Road, 100049 Beijing, China

⁴Department of Physics and Astronomy, McMaster University, Hamilton, Ontario L8S 4M1, Canada

submitted to MNRAS

ABSTRACT

We introduce project NIHAO (Numerical Investigation of a Hundred Astrophysical Objects), a set of 100 cosmological zoom-in hydrodynamical simulations performed using the GASOLINE code, with an improved implementation of the SPH algorithm. The haloes in our study range from dwarf ($M_{200} \sim 5 \times 10^9 M_{\odot}$) to Milky Way ($M_{200} \sim 2 \times 10^{12} M_{\odot}$) masses, and represent an unbiased sampling of merger histories, concentrations and spin parameters. The particle masses and force softenings are chosen to resolve the mass profile to below 1% of the virial radius at all masses, ensuring that galaxy half-light radii are well resolved. Using the same treatment of star formation and stellar feedback for every object, the simulated galaxies reproduce the observed inefficiency of galaxy formation across cosmic time as expressed through the stellar mass vs halo mass relation, and the star formation rate vs stellar mass relation. We thus conclude that stellar feedback is the chief piece of physics required to limit the efficiency of star formation in galaxies less massive than the Milky Way.

Key words: galaxies: evolution – galaxies: formation – galaxies: dwarf – galaxies: spiral – methods: numerical – cosmology: theory

1 INTRODUCTION

Understanding the formation of spiral galaxies (including our own Galaxy – the Milky Way) has been at the forefront of theoretical astrophysics for decades. While there is a broadly-sketched paradigm for the formation of disk galaxies (White & Rees 1978; Fall & Efstathiou 1980; Mo, Mao, & White 1998; Dutton et al. 2007), the details have yet to be understood. The simulation of realistic spiral galaxies from cosmological initial conditions has been a formidable challenge. Early (low-resolution) simulations were plagued by over-cooling, and angular momentum losses resulting in compact bulge dominated galaxies (e.g., Navarro & Steinmetz 2000). Recently, it has been shown that higher spatial resolution coupled to more realistic models for star formation and stellar feedback can solve these problems, resulting in spiral galaxies with realistic sizes and bulge fractions (Guedes et al. 2011; Brook et al. 2012; Aumer et al. 2013; Marinacci et al. 2014; Crain et al. 2015).

One of the most fundamental constraints for galaxy formation models is the relation between the stellar mass of a galaxy, M_{star} , and the mass of its host dark matter halo, M_{halo} . This relation encodes the global efficiency at which galaxies turn gas into stars. In the context of Λ CDM, a model that matches the $M_{\text{star}} - M_{\text{halo}}$ relation will also reproduce the observed galaxy stellar mass function, which has been a benchmark for galaxy formation models for over a decade (e.g., White & Frenk 1991, Benson et al. 2003; Crain et al. 2009; Oppenheimer et al. 2010). An advantage of the M_{star} vs M_{halo} relation is that single galaxies can be compared, whereas comparing with the stellar mass function requires a cosmologically representative volume.

In recent years the M_{star} vs M_{halo} relation has been studied extensively using observations of weak gravitational lensing, satellite kinematics, and halo abundance matching (e.g., Yang et al. 2003, 2012; Mandelbaum et al. 2006; Conroy & Wechsler 2009; Moster et al. 2010; More et al. 2011; Leauthaud et al. 2012; Behroozi et al. 2013; Garrison-Kimmel et al. 2014; Kravtsov et al. 2014; Hudson et al. 2015). One of the key results of these studies is

* lwang@mpia.de

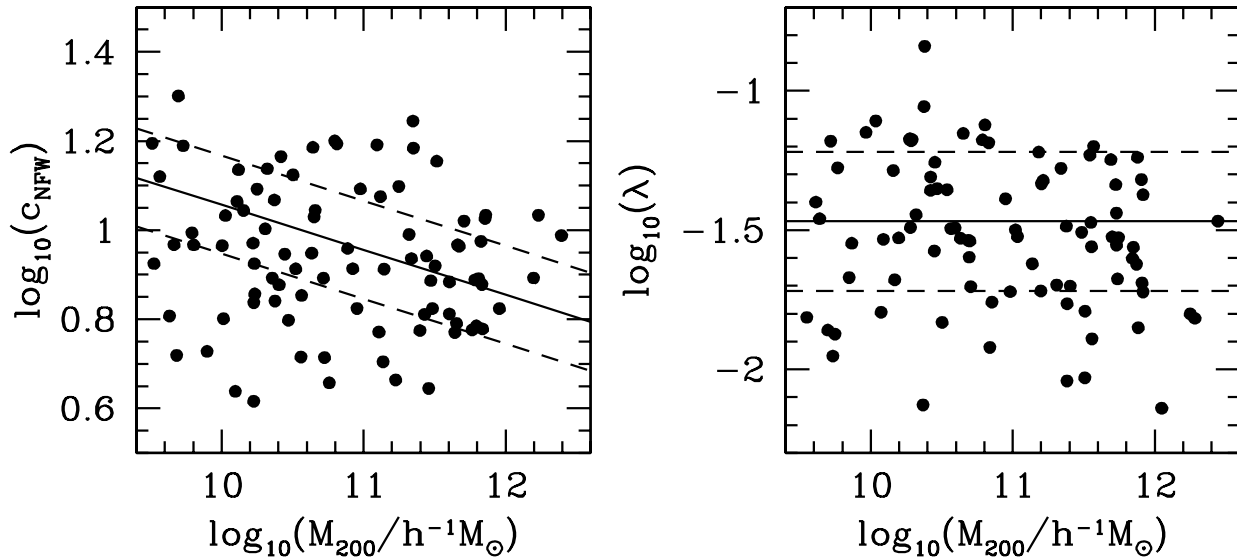


Figure 1. Concentration vs halo mass (left) and spin parameter vs halo mass (right) for the sample of haloes presented in this paper. Concentrations are from NFW fits. Solid and dashed lines show the mean and 1σ scatter from the low-resolution parent simulations in the Planck cosmology from Dutton & Macciò (2014).

that star formation is inefficient – the maximum efficiency is $\sim 25\%$, and independent of redshift, occurring at a halo mass similar to that of the Milky Way (i.e., $\sim 10^{12}M_{\odot}$). At both higher and lower halo masses the efficiency drops even further.

Reproducing this relation both at redshift $z = 0$ and earlier times, in a fully cosmological context has been a challenge, with many simulations and semi-analytic models predicting either too many stars at redshift $z = 0$, or earlier times (Weinmann et al. 2012). Even some of the largest zoom-in and cosmological volume simulations do not reproduce the observed $z = 0$ relation between stellar and halo mass (e.g., Guedes et al. 2011; Marinacci et al. 2014; Vogelsberger et al. 2014). Only a handful of cosmological simulations have been able to match the stellar vs halo mass relation over a wide range of halo masses from dwarfs to the Milky Way (Di Cintio et al. 2014; Hopkins et al. 2014; Schaye et al. 2015). On the other hand these simulations were subject to either limited resolution on disc galaxy scales (Schaye et al. 2015) or based on a handful of objects with unclear selection function (DiCintio et al. 2014; Hopkins et al. 2014) and thus not able to recover the variety of formation histories of real galaxies.

The next step is then to create a large sample of galaxies with very high resolution over a range of halo masses with an unbiased sampling of the mass accretion histories. The NIHAO¹ (Numerical Investigation of a Hundred Astrophysical Objects) project aims to achieve these goals with ~ 100 hydrodynamical cosmological zoom-in simulations with halo masses ranging from $M_{\text{halo}} \sim 5 \times 10^9$ to $\sim 2 \times 10^{12}M_{\odot}$.

In this paper we describe the numerical methods and sample selection and present results on the growth of stellar mass across cosmic time from the first 88 NIHAO simula-

tions. Subsequent papers will discuss: dark halo shapes (Butsky et al. 2015); central dark matter density slopes (Tollet et al. 2015); Tully-Fisher relations (Dutton et al. in prep.); and gas content (Stinson et al. 2015). This paper is organized as follows: The simulations including sample selection, hydrodynamics, star formation and feedback are described in §2, results including the stellar mass vs halo mass and star formation rate vs halo mass relation are presented in §3 and a summary in §4.

2 SIMULATIONS

The simulations presented here are a series of fully cosmological “zoom-in” simulations of galaxy formation run in a flat Λ CDM cosmology with parameters from the Planck Collaboration et al. (2014): Hubble parameter $H_0 = 67.1 \text{ km s}^{-1} \text{ Mpc}^{-1}$, matter density $\Omega_m = 0.3175$, dark energy density $\Omega_{\Lambda} = 1 - \Omega_m - \Omega_r = 0.6824$, radiation density $\Omega_r = 0.00008$, baryon density $\Omega_b = 0.0490$, power spectrum normalization $\sigma_8 = 0.8344$, power spectrum slope $n = 0.9624$.

2.1 Sample selection and Initial Conditions

The simulated galaxies were selected from two cosmological boxes of sides 60 and 20 Mpc/h from Dutton & Macciò (2014), as well as a new simulation of size 15 Mpc/h with 400^3 particles. We select halo masses from $9.5 \lesssim \log_{10}(M_{200}/M_{\odot}) \lesssim 12.3$. Haloes are selected without considering the halo structure or merger history. For technical reasons with the zoom-in technique we require the haloes to be “isolated”. Formally, we only consider haloes that have no other haloes with mass greater than one-fifth of the virial mass within 3 virial radii. 95% of all parent haloes satisfy this constraint, so it does not bias our sample in any significant way. The concentration vs mass and spin vs mass

¹ Nihao is the Chinese word for “hello”.

Table 1. Dark and gas particle masses, m , and force softenings, ϵ , for our zoom-in simulations.

box.level	halo mass range (M_{\odot})	m_{gas} (M_{\odot})	ϵ_{gas} (pc)	m_{DM} (M_{\odot})	ϵ_{DM} (pc)
60.1	$6.96 \times 10^{11} - 2.79 \times 10^{12}$	3.166×10^5	397.9	1.735×10^6	931.4
60.2	$8.89 \times 10^{10} - 5.55 \times 10^{11}$	3.958×10^4	199.0	2.169×10^5	465.7
60.3	$2.63 \times 10^{10} - 7.12 \times 10^{10}$	1.173×10^4	132.6	6.426×10^4	310.5
20.1	$4.99 \times 10^9 - 2.94 \times 10^{10}$	3.475×10^3	88.4	1.904×10^4	207.0
15.1	$5.41 \times 10^9 - 9.26 \times 10^9$	2.087×10^3	74.6	1.144×10^4	174.6
20.2	4.36×10^9	1.466×10^3	66.4	8.032×10^3	155.2
15.2	3.54×10^9	6.184×10^2	49.7	3.389×10^3	116.4

relations from dark matter only simulations are shown in Fig. 1. The solid and dashed lines show the mean and scatter from the parent simulations from Dutton & Macciò (2014) showing that our selected haloes span a wide range in concentrations and spins.

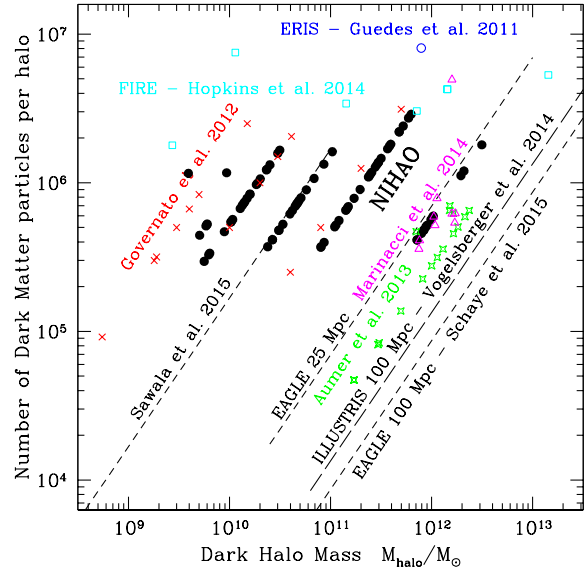
Initial conditions for zoom-in simulations were created using a modified version of the GRAFIC2 package (Bertschinger 2001) as described in Penzo et al. (2014). We chose the refinement level in order to maintain a roughly constant relative resolution (i.e., $\epsilon_{\text{DM}}/R_{\text{vir}} \sim 0.003$), and $\sim 10^6$ dark matter particles per halo. This allows us to reliably probe the mass profile down to 1% of the virial radius or better across the full range of halo masses we simulate. The motivation for achieving a constant relative resolution, rather than a fixed physical resolution is that we wish to resolve the dark matter mass profile down to the galaxy half-light radius, which is typically 1-2% of the virial radius (Kravtsov 2013).

Fig. 2 shows the mass resolution of our simulations compared to a number of state-of-the-art zoom-in (ERIS - Guedes et al. 2011; Governato et al. 2012; Aumer et al. 2013; Marinacci et al. 2014; FIRE - Hopkins et al. 2014; Sawala et al. 2015) and large volume (ILLUSTRIS - Vogelsberger et al. 2014; EAGLE - Schaye et al. 2015) simulations. NIHAO is by far the largest set of zoom-in simulations resolved with $\sim 10^6$ particles per halo. The large volume simulations (EAGLE, ILLUSTRIS) contain many thousands of galaxies, but the fixed force and mass resolution means that only the highest mass haloes are well resolved.

The force softenings and particle masses for the highest refinement level for each simulation are given in Table 1. Note that the ratio between dark and gas particle masses is initially the same as the cosmological dark/baryon mass ratio $\Omega_{\text{DM}}/\Omega_{\text{b}} \approx 5.48$, and the gas (and star) particle force softenings are set to be $\sqrt{(\Omega_{\text{DM}}/\Omega_{\text{b}})} \approx 2.34$ times smaller than the dark matter particle softenings. Each hydrodynamic simulation has a corresponding dark matter-only simulation run at the same mass and force resolution to enable a study of the effects of galaxy formation on dark halo structure (Dutton et al. in prep).

2.2 Hydrodynamics

We use a new version of the N-body SPH solver GASOLINE (Wadsley et al. 2004). A complete description of the new gasoline code including tests is given in Wadsley et al. (in prep.). In their paper describing superbubble feedback, Keller et al. (2014) described the updates they made to


Figure 2. Number of dark matter particles per halo vs halo mass for NIHAO simulations (black circles) together with state-of-the-art cosmological simulations in the literature.

GASOLINE. While we do not use their superbubble feedback, we employ their modified version of hydrodynamics that reduces the formation of blobs and improves mixing. We thus refer to our version of GASOLINE as ESF-GASOLINE2. The biggest differences to the hydrodynamics in ESF-GASOLINE2 come from the small change Ritchie & Thomas (2001) proposed for calculating P/ρ^2 . Ritchie & Thomas (2001) also proposed modifying the density calculation to use equal pressures, but we do *not* use those densities in the simulations described here.

Diffusion of quantities like metals and thermal energy between particles has been implemented as described in Wadsley et al. (2008). Metal diffusion is used, but thermal diffusion is not used because it is incompatible with the blastwave feedback that delays cooling. GASOLINE2 includes several other changes to the hydrodynamic calculation. The Saitoh & Makino (2009) timestep limiter was implemented so that cool particles behave correctly when a hot blastwave hits them. To avoid pair instabilities, ESF-GASOLINE2 uses the Wendland C^2 function for its smoothing kernel (Dehnen & Aly 2012). The treatment of artificial viscosity has been modified to use the signal velocity as described in Price

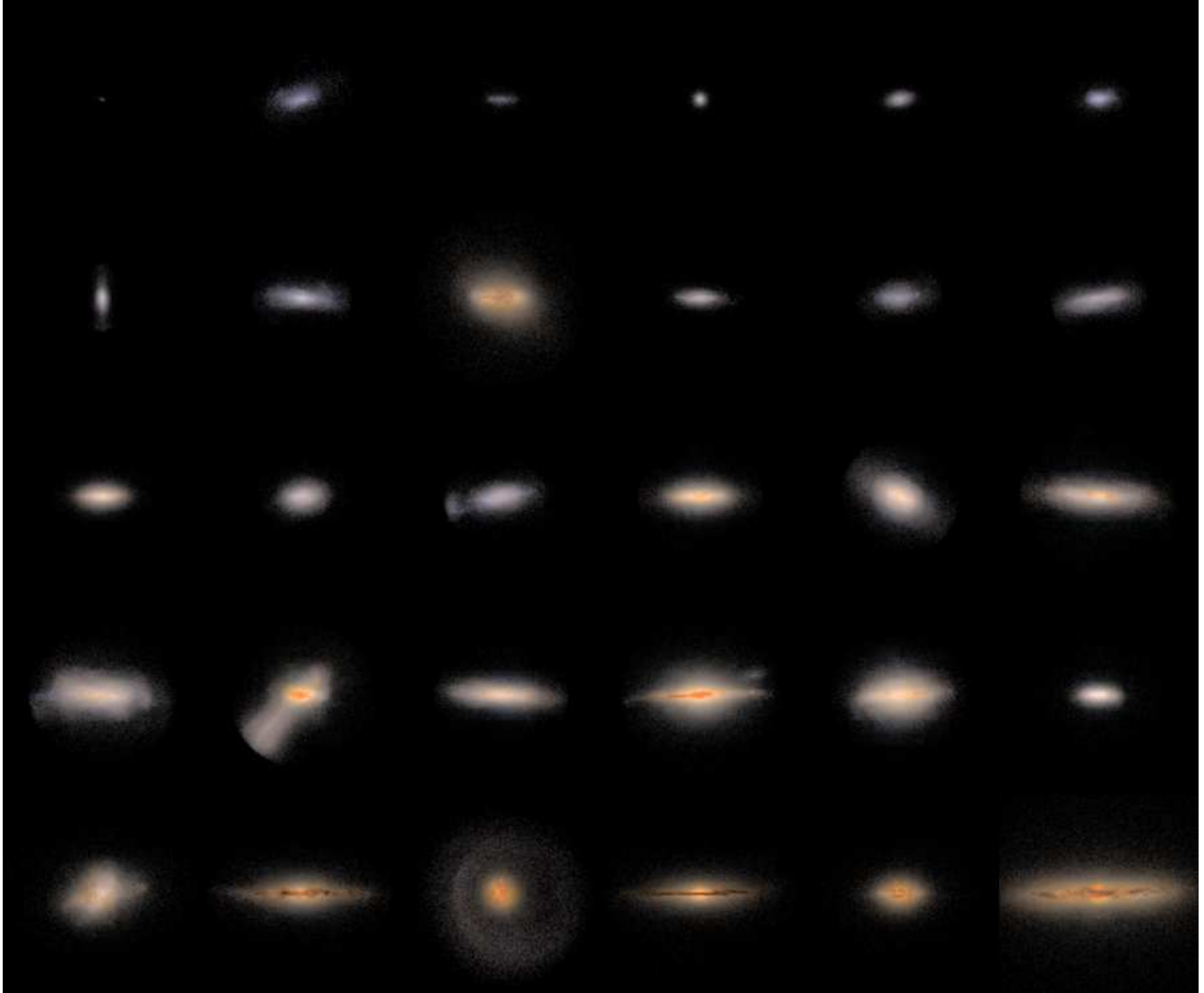


Figure 3. Edge-on views of a subset of NIHAO galaxies after processing through the Monte Carlo radiative transfer code SUNRISE. Images are 50 kpc on a side.

(2008). We also increase the number of neighbor particles used in the calculation of the smoothed hydrodynamic properties from 32 to 50.

Cooling via hydrogen, helium, and various metal-lines in a uniform ultraviolet ionizing background is included as described in Shen et al. (2010) and was calculated using CLOUDY (version 07.02; Ferland et al. 1998). These calculations include photo ionization and heating from the Haardt & Madau (private communication) UV background and Compton cooling and range from 10 to 10^9 K. In the dense interstellar medium gas the extragalactic UV field is a reasonable approximation, and thus we do not impose any shielding.

2.3 Star Formation and Feedback

Within the hydrodynamic simulations, gas is eligible to form stars according to the Kennicutt-Schmidt Law when it satisfies a temperature and density threshold. Our fiducial runs adopt $T < 15000$ K and $n_{\text{th}} > 10.3 \text{ cm}^{-3}$. The stars feed

energy back into the interstellar medium (ISM) gas through blast-wave supernova feedback (Stinson et al. 2006) and ionizing feedback from massive stars prior to their explosion as supernovae, referred to as “early stellar feedback” (Stinson et al. 2013).

In GASOLINE, as in Stinson et al. (2013), the pre-SN feedback consists of $\epsilon_{\text{ESF}} = 10\%$ of the total stellar flux, 2×10^{50} erg of thermal energy per M_{\odot} of the entire stellar population, being ejected from stars into surrounding gas. Because of the increased mixing in ESF-GASOLINE2, the simulations required more stellar feedback to have their star formation limited to the abundance matching value at the Milky Way scale. Thus, we set $\epsilon_{\text{ESF}} = 13\%$, which gives a better match to Behroozi et al. (2013) abundance matching results. Radiative cooling is left *on* for the pre-SN feedback.

In the second, supernova, epoch of feedback, stars of mass $8 M_{\odot} < M_{\text{star}} < 40 M_{\odot}$ eject both energy and metals into the interstellar medium gas surrounding the region where they formed. Supernova feedback is implemented using the blastwave formalism described in Stinson

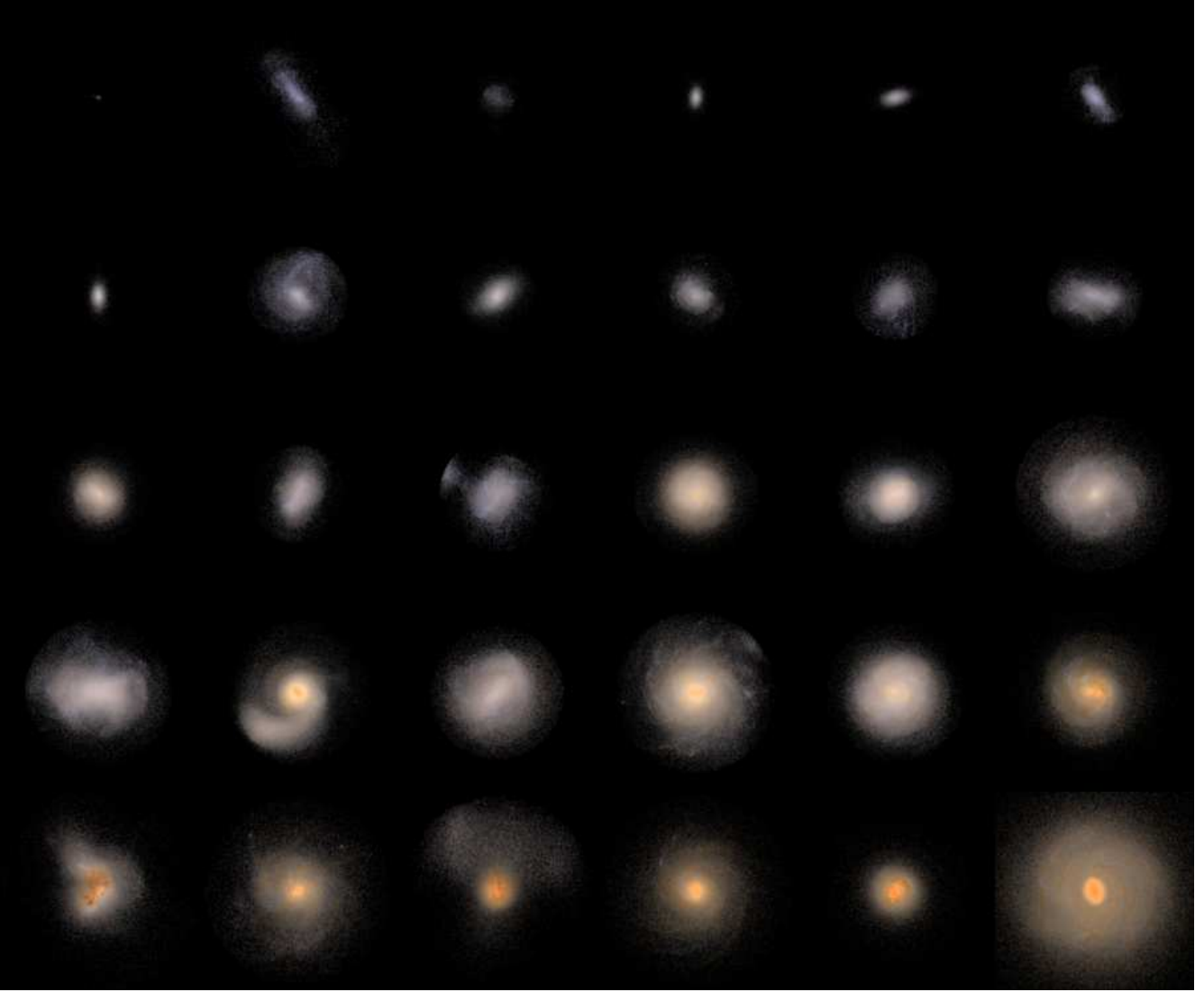


Figure 4. Face-on views of a subset of NIHAO galaxies after processing through the Monte Carlo radiative transfer code SUNRISE. Images are 50 kpc on a side.

et al. (2006). Since the gas receiving the energy is dense, it would quickly be radiated away due to its efficient cooling. For this reason, cooling is delayed for particles inside the blast region for ~ 30 Myr.

2.4 Derived galaxy and halo parameters

In this section we describe how the various galaxy and halo parameters we use in the rest of the paper are defined and measured.

Haloos in our zoom-in simulations were identified using the MPI+OpenMP hybrid halo finder **AHF**² (Knollmann & Knebe 2009; Gill et al. 2004). **AHF** locates local over-densities in an adaptively smoothed density field as prospective halo centers. The virial masses of the haloos are defined as the masses within a sphere containing $\Delta = 200$ times the cosmic critical matter density. The virial mass, and size are denoted

M_{200} and R_{200} . The mass in stars, M_{star} , is measured within a sphere of radius, $r_{\text{gal}} \equiv 0.2R_{200}$. The star formation rate, SFR, is measured as the mass of stars formed inside r_{gal} over the preceding 100 Myr. These parameters of the main halo/galaxy are given in Table A1. The simulation ID is named after the redshift $z = 0$ halo mass ($M_{\text{vir}}/[M_{\odot}/h]$) from the low resolution dark matter-only simulation. The actual halo masses in the hydrodynamic simulation may differ due to: baryonic mass loss; differential evolution; and a different halo mass definition.

Edge-on and face-on images for a selection of 30 galaxies at $z = 0$ are shown in Figs. 3 & 4. Each image is 50 kpc on a side and was created using the Monte Carlo radiative transfer code **SUNRISE** (Jonsson 2006). The image brightness and contrast are scaled using arcsinh as described in Lupton et al. (2004). The image orientation was determined using the angular momentum vector of the stars inside 5 kpc. We see a variety of galaxy morphologies, sizes, colors, and bulge-to-disc ratios. The galaxies are ordered according to their halo masses. The variation in morphology follows the

² <http://popia.ft.uam.es/AMIGA>

increase of halo mass. The lowest mass galaxies are small blue dots. Higher mass halos gradually extend into peanut shapes before filling out entire discs. Once the galaxies become discs, their stellar populations start to include more old, red stars, and exhibit stronger absorption from dust lanes. These discs then start to show extended merger structures. In some cases the disc has disappeared and all that is left is a smaller, red spheroid that represents the remnant of a merger. Even though all the images are taken from the $z = 0$ outputs, the mass sequence seems to replicate the evolutionary sequence of galaxies.

In addition to the main target halo each simulation contains several smaller haloes within the high-res region, which we include in our analysis. We verify with convergence tests (see §3 below) that these poorer resolved haloes have similar global parameters to their higher resolution counterparts.

3 RESULTS

3.1 Stellar mass vs halo mass

Fig. 5 shows the relation between stellar mass and virial mass for our simulated central galaxies compared to results from three different halo abundance matching measurements: Behroozi et al. (2013), Moster et al. (2013), and Kravtsov et al. (2014). We show all three relations to represent the lingering uncertainty in the abundance matching and halo occupation techniques. Most of the difference is apparent at low stellar masses, $M_{\text{star}} \lesssim 10^8 M_{\odot}$. That is the lower mass limit for the Sloan Digital Sky Survey (SDSS, Blanton et al. 2005). The smaller, deeper survey, GAMA (Driver et al. 2012), has pushed the stellar mass function to lower masses, but only the Kravtsov line uses data from the most up-to-date GAMA survey. The lines at low masses are dashed indicating that they are extrapolations of the higher mass results. The Kravtsov relation also differs from the other two at high masses because of how it takes into account intra-cluster light, namely by using the Bernardi et al. (2013) stellar mass function that extends surface brightness profiles to larger radii. Our simulations agree well with each of these relations, especially the most up-to-date relation from Kravtsov et al. (2014) at high masses. At low masses, the simulations most closely follow the extrapolation of the Moster et al. (2013), which has the steepest slope, $M_{\text{star}} \propto M_{200}^{2.4}$.

An additional systematic uncertainty to consider is due to form of the stellar initial mass function (IMF). The abundance matching results use stellar masses assuming a universal Milky Way IMF (e.g., Chabrier 2003). A Milky Way IMF in spiral galaxies is consistent with dynamical based mass-to-light ratios (Courteau & Dutton 2015). However, there is increasing evidence for “heavier” IMFs in massive elliptical galaxies and the bulges of massive spiral galaxies (e.g., Conroy & van Dokkum 2012; Dutton et al. 2013a,b). These studies suggest that for massive galaxies ($M_{\text{star}} \gtrsim 10^{11} M_{\odot}$) the observed stellar masses may be underestimated by a factor of ~ 2 when assuming a Milky Way IMF and standard stellar population models. Taking this into consideration nominally improves the agreement of our most massive simulations with observations. Note that formally we should use the same IMF in the observations and simulations. However, practically speaking the feedback efficiency parameters

in the simulations can be simply rescaled. In addition, there is enough observational uncertainty in the high mass end of the IMF, as well as the actual energy released per SN that this inconsistency is not significant.

The parameters of the feedback model are kept constant across the entire mass range. The parameters were determined based on a comparison with abundance matching for one galaxy about the mass of the Milky Way ($M_{200} \sim 10^{12} M_{\odot}$) (see Stinson et al. 2013). The agreement between the simulated galaxies and the abundance matching at a wide range of masses provides strong support for stellar feedback being the key ingredient that limits star formation in galaxies lower mass than the Milky Way (see also Hopkins et al. 2014).

The points in Fig. 5 are color coded according to the number of particles within the virial radius (dark, gas and stars). The main haloes have between 4×10^5 and 4×10^6 particles. The halo mass range from 2×10^{10} to $10^{11} M_{\odot}$ includes simulations with a wide range of resolutions (from 20 000 to more than 400 000 particles, and dark matter particles’ mass is from 6.4×10^4 to $1.7 \times 10^6 M_{\odot}$). There are no systematic offsets indicating good convergence in stellar masses at an order of magnitude fewer particles than our zoom-in target galaxies. In addition, our central galaxies have a range of physical spatial resolutions, with baryonic force softenings varying from 50 pc to 400 pc. This is encouraging as cosmological simulations do not always converge when changing the physical resolution (see discussions in Vogelsberger et al. 2014; Schaye et al. 2015).

Below a halo mass of $M_{200} \sim 2 \times 10^{10} M_{\odot}$, there starts to be a discrepancy between different resolutions. The high resolution simulations (blue points) contain less stars than lower resolution galaxies. There are two possibilities: Stars may form more readily in low resolution galaxies or else their halo masses might be reduced through environmental processes such as tidal stripping. While the lower resolution halos are outside of the main halos in the $z = 0$ output, it is possible that they have flown nearby the main galaxy at some point in the past given their proximity to more massive halos. The low resolution halo could form a mass of stars according to its earlier halo mass, make a close passage of the main halo, and thus have its halo mass reduced while retaining its stellar mass (for a study that shows that the outermost mass is stripped first, see Chang et al. 2013).

Above a halo mass of $M_{200} \sim 2 \times 10^{10} M_{\odot}$ the scatter in the relation is a constant and consistent with observational constraints of ~ 0.2 dex (More et al. 2011; Reddick et al. 2013). Below a halo mass of $M_{200} \sim 2 \times 10^{10} M_{\odot}$ the scatter starts to increase. More high resolution simulations are needed to verify if this feature is due to the relatively low resolution of these haloes or environmental effects.

A number of semi-analytic models have been able to produce galaxies that follow the observed relation between stellar and halo mass at redshift $z \sim 0$ (e.g., Bower et al. 2006; Somerville et al. 2008; Guo et al. 2011). However, simultaneously reproducing the evolution has been a challenge (Weinmann et al. 2012; Hopkins et al. 2014). Fig. 6 shows the evolution of the stellar mass vs halo mass relation since redshift $z = 4$ (a look back time of ~ 12 Gyr). Here we only show the most massive halo per simulation. Our simulations show good agreement with the abundance matching relations from Behroozi et al. (2013) and Moster

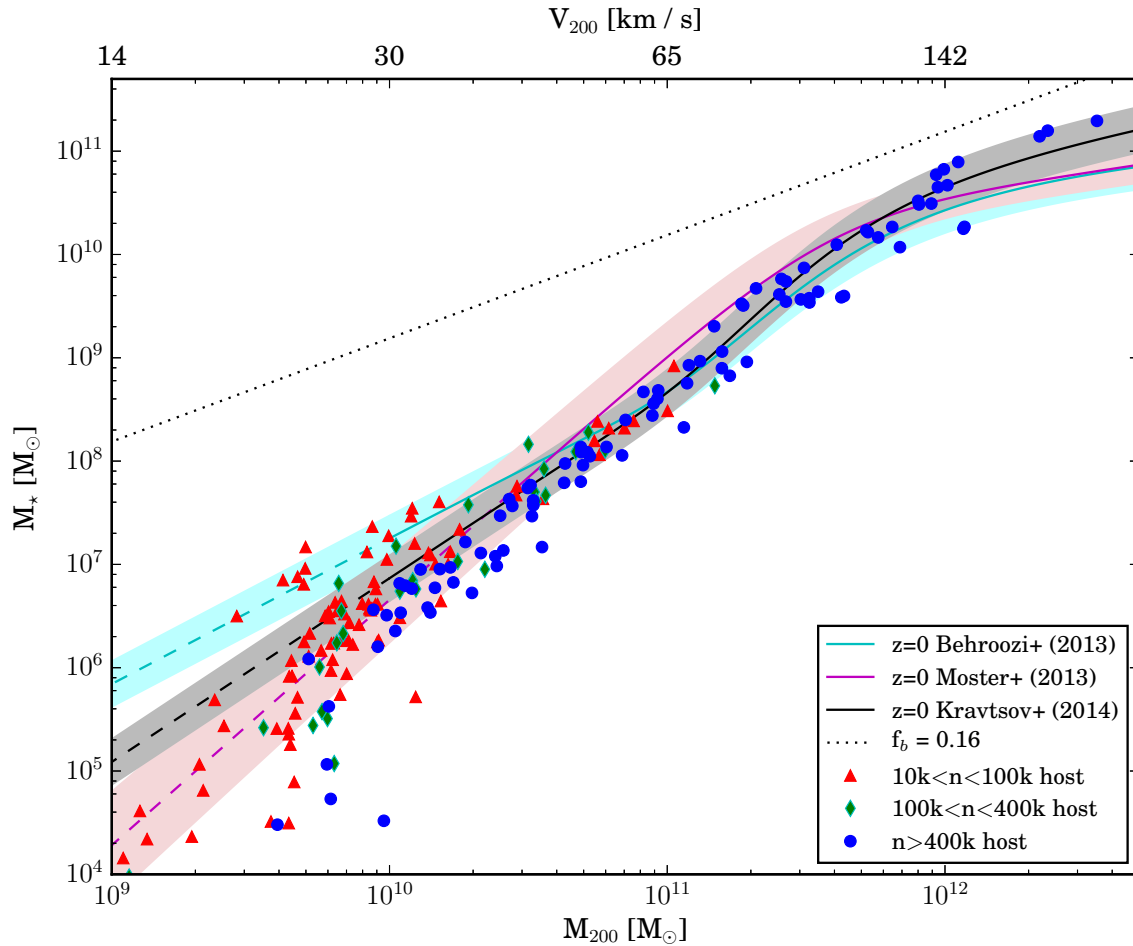


Figure 5. Stellar mass vs halo mass at redshift $z = 0$ for main simulations (blue points) together with lower mass galaxies in the zoom-in region (green and red points). The solid black line and shaded region shows the relation from Kravtsov et al. (2014) derived using halo abundance matching. Our simulation matches this very well. The dashed lines show extrapolations of the abundance matching relations. For reference, the dotted line shows the cosmic baryon fraction of mass associated with the dark matter halo, indicating that our simulations convert only a small fraction of the available gas into stars, as observed.

et al. (2013). Note that most of the simulated galaxies fall in a mass range that can only be extrapolated (dashed lines). The range of masses directly constrained by observations is shown as the solid lines.

The agreement with the $M_{\text{star}} - M_{200}$ relation is not totally unexpected, as the feedback model employed here has been shown to reproduce the time evolution of a single Milky Way mass galaxy through the stellar mass vs halo mass plane (Stinson et al. 2013), as well as the stellar to halo mass relation for galaxies of mass $10^{8.5} \lesssim M_{\text{star}} \lesssim 10^{10.5} M_{\odot}$ at redshifts $z > 2$ using lower resolution simulations in a cosmological volume of size ~ 100 Mpc (Kannan et al. 2014). Our study bridges the gap between these two works by creating a large number of high-resolution simulations with realistic stellar masses.

Our simulations are not the first to replicate the $M_{\text{star}} - M_{\text{halo}}$ relation at $z = 0$ or even at higher redshifts. Aumer et al. (2013) presented a sample of 16 galaxies with comparable resolution to those presented here but on a smaller mass range ($10^{11} M_{\odot}$ to $2 \times 10^{12} M_{\odot}$). Those simulations showed a similar mass and redshift dependence as the sim-

ulations presented in our sample, even though they tend to over produce stars at $z > 4$ and under produce them at $z < 0.5$ in the low mass range, an effect we do not see in our (even larger) sample.

Hopkins et al. (2014) presented a sample of only 7 galaxies with a factor of ~ 5 higher mass resolution than ours (see Fig. 2), accompanied by several other galaxies that were also simulated inside the zoom region. Again, the results are similar to what we find, although at all halo masses they over-produce stellar masses at $z = 2$ when compared with the Behroozi et al. (2013) prediction and its extrapolation. All three simulation suites were run with different codes and stellar feedback recipes, but there are common features to all of them. 1) They all include efficient supernova feedback (at least 10^{51} erg returned to the ISM in all cases). 2) The supernova feedback is deposited in the local environment of where the stars formed, promptly, ~ 3 Myr after the stars formed. 3) They all include some sort of feedback prior to supernova (Aumer: strong, $\tau_{\text{IR}} \sim 25$, radiation pressure; Hopkins: radiation pressure, stellar winds, and photoioniza-

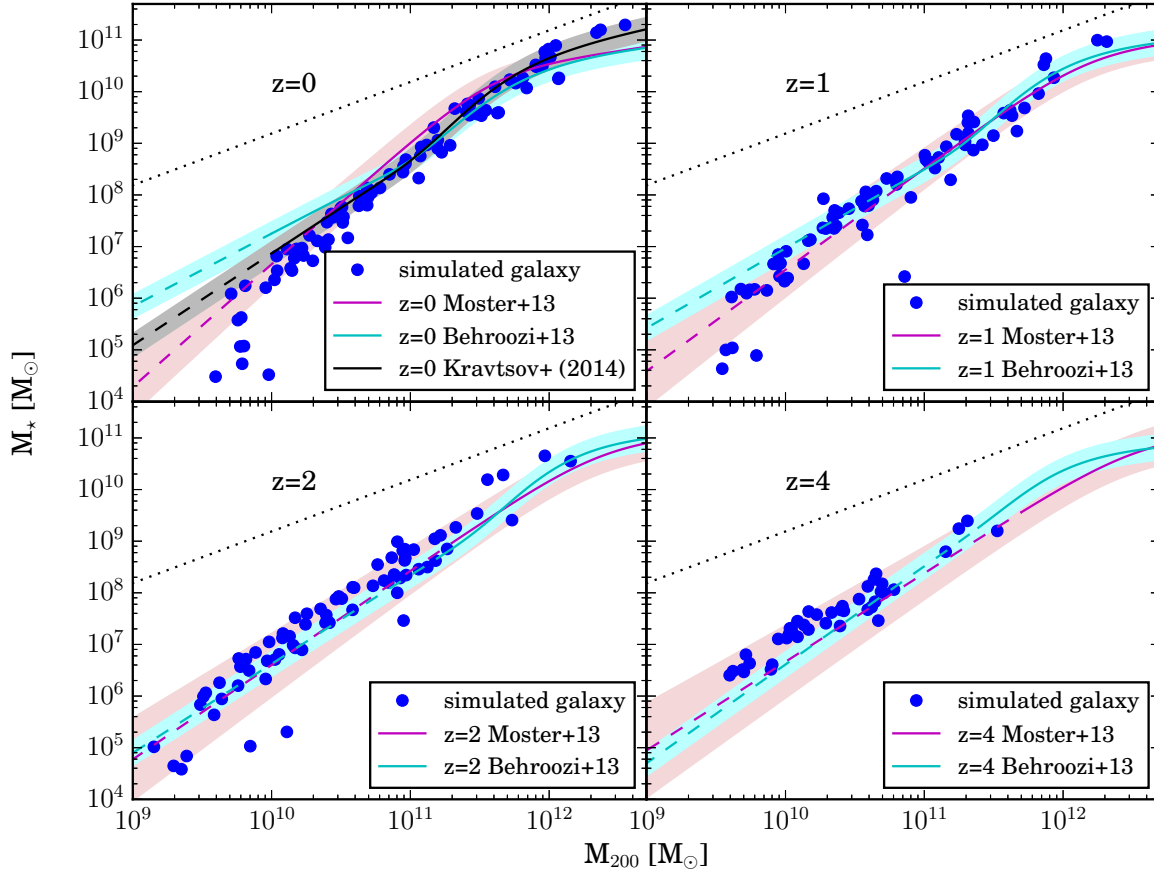


Figure 6. Evolution of the Stellar mass vs halo mass relation. Redshift $z = 0$ (top left), $z = 1$ (top right), $z = 2$ (bottom left), and $z = 4$ (bottom right). Only the most massive halo in each zoom-in region are shown. There is good agreement between our simulations and constraints from halo abundance matching (Moster et al. 2013; Behroozi et al. 2013). The dashed lines show extrapolation of the relations into mass scales without observational constraints. For reference, the dotted line shows the cosmic baryon fraction of mass associated with the dark matter halo.

tion; this work: strong photoionization included as thermal energy).

Schaye et al. (2015) shows that their simulated stellar mass function follows observations at $z = 0$, with an exception at the knee that translates into a low peak efficiency of star formation around $M_{\text{halo}} \sim 10^{12} M_{\odot}$ (see their figure 8). Those simulations invoke a simple prescription for stellar feedback that injects slightly more thermal energy per supernova instantaneously after the star particle is formed. They add AGN feedback to their energy budget, which prevents over cooling in higher mass galaxies.

3.2 Star formation rate vs stellar mass

A consistency check on the stellar mass growth of our simulated galaxies comes from the relation between star formation rate and stellar mass, sometimes referred to as the “star forming main sequence.”

Fig. 7 shows the evolution of the star forming main sequence in our simulations compared with the observed relations (as compiled by Dutton et al. 2010) at $z \sim 0$ (Elbaz

et al. 2007, Salim et al. 2007), $z \sim 1$ (Elbaz et al. 2007, Noeske et al. 2007), $z \sim 2$ (Daddi et al. 2007) and $z \sim 4$ (Daddi et al. 2009, Stark et al. 2009), together with the compilation by Behroozi et al. (2013). Broadly speaking, our simulations recover the order of magnitude decline in SFR at fixed stellar mass observed since $z \sim 4$. In more detail, they match the observations well at all but the lowest mass bins, where the observations are more prone to selection biases.

The agreement at redshift $z = 2$ is especially noteworthy, as a common feature of galaxy formation models is to underpredict the observed SFRs by a factor of $\gtrsim 2$ (e.g., Dutton et al. 2010; Yang et al. 2013; Romeo Veloná et al. 2013; Somerville & Davé 2014; Furlong et al. 2015). This feature of previous models is due to a strong coupling between the cosmological gas accretion and star formation rates (Weinmann et al. 2011) which leads to $SSFR \propto (1+z)^{2.25}$. In our simulations this coupling is broken by our feedback model, which effectively delays star formation at early times. Other solutions have included a modification to the stellar IMF (Davé 2008) or an appeal to systematic bi-

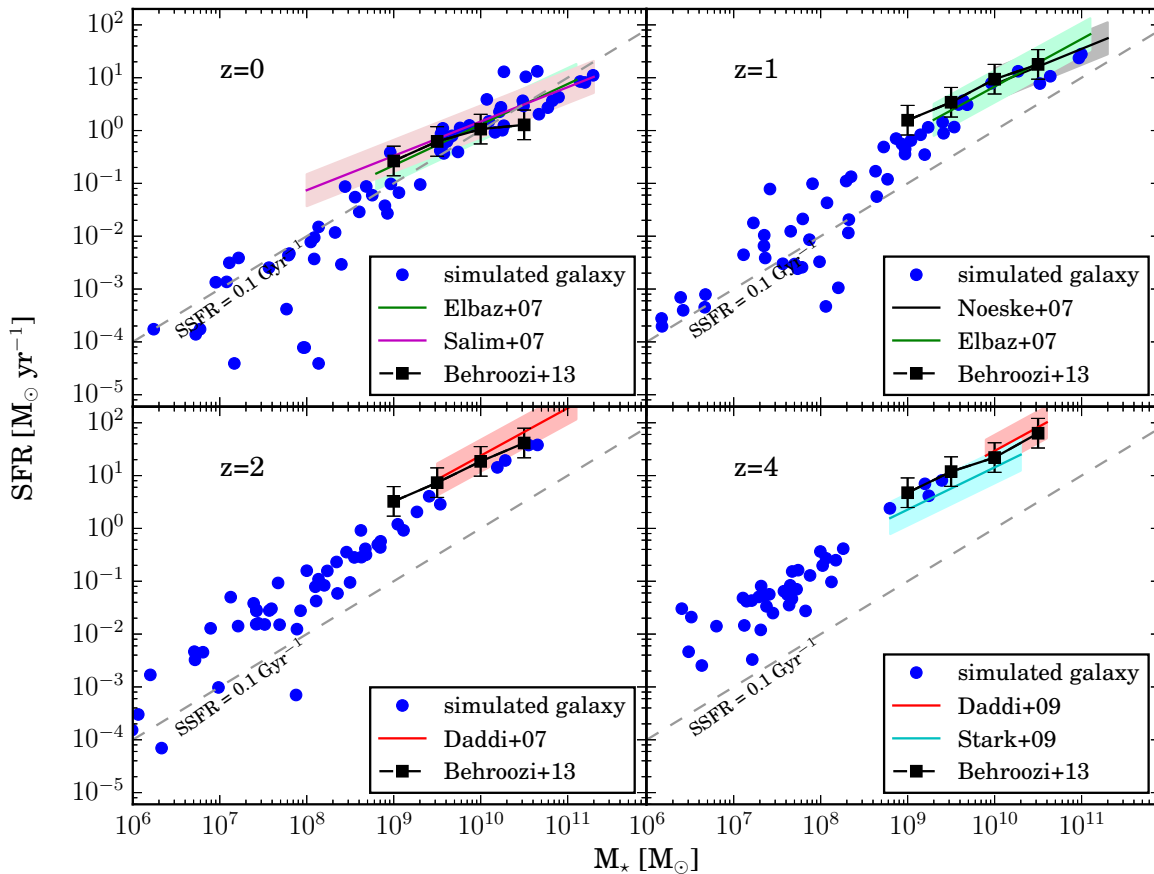


Figure 7. Evolution of the galaxy star formation rate vs stellar mass relation. NIHAO simulations are shown with blue points, observed relations by lines and shaded regions as indicated. For reference the dashed lines show a specific star formation rate, $\text{SSFR} = \text{SFR}/M_{\text{star}} = 0.1 \text{ Gyr}^{-1}$. The average SSFR of our simulations decline by a factor of ~ 30 from $z = 4$ to the present day.

ases in the observed star formation rates and stellar masses which could plausibly be at the factor of ~ 2 level.

3.3 Rotation curves

To this point, our analysis has focused exclusively on the mass of stars formed in the simulated haloes. Those comparisons show that our simulations are successful according to that measure. However, a fully successful galaxy formation model should also reproduce the mass *distribution* of material in the galaxies. We will look into the matter distributions in more depth in follow-up papers, but give a preliminary look at the rotation curves for the simulated galaxies here.

Fig. 8 shows the spherically averaged circular velocities for all the galaxies in the NIHAO sample. The galaxies have been separated into four separate mass groups to limit the confusion. The circular velocity curves are colored by their halo mass. The curves show a gradual transition based on mass that represents a change in the halo response that will be explored more explicitly in Dutton et al. (*in prep*). In gen-

eral terms, the lowest mass halos, $M_{200} < 2 \times 10^{10} M_{\odot}$, have rotation curves that rise relatively steeply. As the masses increase, the rotation curves rise more slowly. Then, the galaxies cross a higher mass threshold around $6 \times 10^{11} M_{\odot}$ at which the galaxies revert to a steeply rising rotation curve, which in some cases grows to have a high central peak. Such centrally peaked rotation curves do exist in observed massive spiral galaxies (e.g., Noordermeer et al. 2007; Dutton et al. 2013a). However, we note that our simulations do not include any form of AGN feedback. The central peaks in the rotation curves may thus represent over cooling that would otherwise be heated by AGN or another higher energy phenomenon.

4 SUMMARY

We introduce a new, unmatched sample of high resolution hydrodynamic simulations from the NIHAO project. The galaxies are individually simulated in their own zoom regions. They span a wide range of halo masses, $5 \times 10^9 < M_{200}/M_{\odot} < 3 \times 10^{12}$ and stellar masses $5 \times 10^4 <$

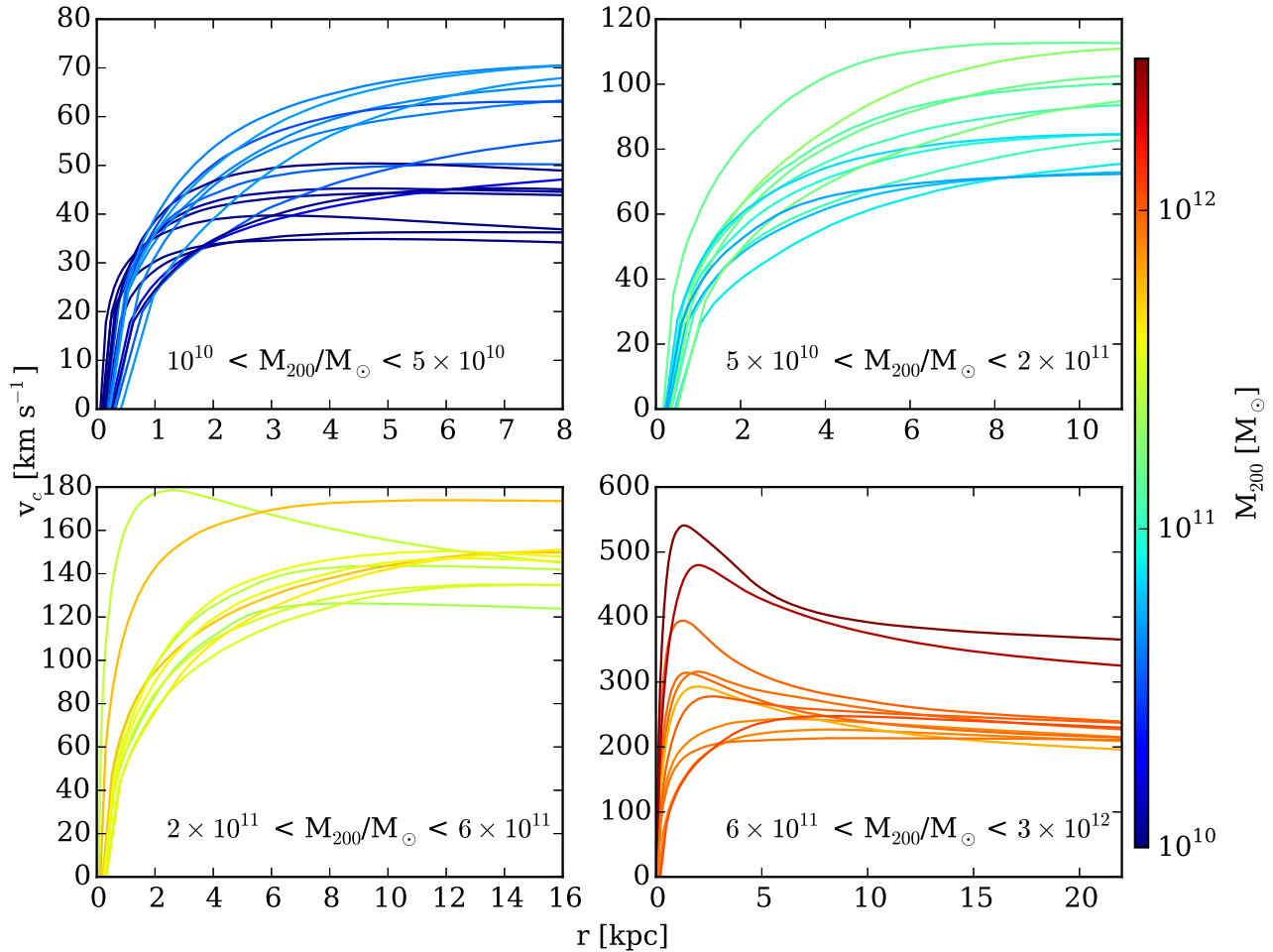


Figure 8. Rotation curves of the spherically averaged circular velocity $\sqrt{GM/r}$, split into four halo mass ranges, as indicated.

$M_{\text{star}}/M_{\odot} < 2 \times 10^{11}$. Across this range of masses, the galaxies show a range of morphologies, colors and sizes that correspond well with observed galaxies. The only energetic source term for the simulations comes from stars: stellar feedback due to photoionization from hot, young stars; and the thermal energy from supernovae. The stellar masses of the simulations closely track the results from abundance matching for stellar masses as a function of halo mass across more than three quarters of the life of the Universe. That means that a complete cosmological sample of these galaxies would populate the stellar mass function as observed. The correspondence of the simulations to observations provides a final proof that stellar feedback is the chief piece of physics required to limit the efficiency of star formation in galaxies less massive than the Milky Way.

ACKNOWLEDGMENTS

The analysis was performed using the PYNBODY package (Pontzen et al. 2013), which had key contributions from Andrew Pontzen and Rok Roškar in addition to the authors. The simulations were performed on the theo cluster of the Max-Planck-Institut für Astronomie and the hydra

cluster at the Rechenzentrum in Garching; and the Milky Way supercomputer, funded by the Deutsche Forschungsgemeinschaft (DFG) through Collaborative Research Center (SFB 881) “The Milky Way System” (subproject Z2), hosted and co-funded by the Jülich Supercomputing Center (JSC). We greatly appreciate the contributions of all these computing allocations. AAD, AVM, and GSS acknowledge support through the Sonderforschungsbereich SFB 881 “The Milky Way System” (subprojects A1 and A2) of the German Research Foundation (DFG). The authors acknowledge support from the MPG-CAS through the partnership programme between the MPIA group lead by AVM and the PMO group lead by XK. LW acknowledges support of the MPG-CAS student programme. XK acknowledges the support from NSFC project No.11333008 and the “Strategic Priority Research Program the Emergence of Cosmological Structures” of the CAS(No.XD09010000). GSS acknowledges funding from the European Research Council under the European Union’s Seventh Framework Programme (FP 7) ERC Grant Agreement n. [321035].

REFERENCES

- Aumer, M., White, S. D. M., Naab, T., & Scannapieco, C. 2013, *MNRAS*, 434, 3142
- Behroozi, P. S., Wechsler, R. H., & Conroy, C. 2013, *ApJ*, 770, 57
- Benson, A. J., Bower, R. G., Frenk, C. S., et al. 2003, *ApJ*, 599, 38
- Bernardi, M., Meert, A., Sheth, R. K., et al. 2013, *MNRAS*, 436, 697
- Bertschinger, E. 2001, *ApJS*, 137, 1
- Blanton, M. R., Lupton, R. H., Schlegel, D. J., et al. 2005, *ApJ*, 631, 208
- Bower, R. G., Benson, A. J., Malbon, R., et al. 2006, *MNRAS*, 370, 645
- Brook, C. B., Stinson, G., Gibson, B. K., Wadsley, J., & Quinn, T. 2012, *MNRAS*, 424, 1275
- Butsky, I., Macciò, A. V., Dutton, A. A., et al. 2015, *arXiv:1503.04814*
- Chabrier, G. 2003, *PASP*, 115, 763
- Chang, J., Macciò, A. V., & Kang, X. 2013, *MNRAS*, 431, 3533
- Conroy, C., & Wechsler, R. H. 2009, *ApJ*, 696, 620
- Conroy, C., & van Dokkum, P. G. 2012, *ApJ*, 760, 71
- Courteau, S., & Dutton, A. A. 2015, *ApJL*, 801, L20
- Crain, R. A., Theuns, T., Dalla Vecchia, C., et al. 2009, *MNRAS*, 399, 1773
- Crain, R. A., Schaye, Y., Bower, R. G., et al. 2015, *MNRAS*, 450, 1937
- Daddi, E., Dickinson, M., Morrison, G., et al. 2007, *ApJ*, 670, 156
- Daddi, E., Dannerbauer, H., Stern, D., et al. 2009, *ApJ*, 694, 1517
- Davé, R. 2008, *MNRAS*, 385, 147
- Dehnen, W., & Aly, H. 2012, *MNRAS*, 425, 1068
- Di Cintio, A., Brook, C. B., Macciò, A. V., et al. 2014, *MNRAS*, 437, 415
- Driver, S. P., Robotham, A. S. G., Kelvin, L., et al. 2012, *MNRAS*, 427, 3244
- Dutton, A. A., van den Bosch, F. C., Dekel, A., & Courteau, S. 2007, *ApJ*, 654, 27
- Dutton, A. A., van den Bosch, F. C., & Dekel, A. 2010, *MNRAS*, 405, 1690
- Dutton, A. A., Treu, T., Brewer, B. J., et al. 2013a, *MNRAS*, 428, 3183
- Dutton, A. A., Macciò, A. V., Mendel, J. T., & Simard, L. 2013b, *MNRAS*, 432, 2496
- Dutton, A. A., & Macciò, A. V. 2014, *MNRAS*, 441, 3359
- Elbaz, D., Daddi, E., Le Borgne, D., et al. 2007, *A&A*, 468, 33
- Fall, S. M., & Efstathiou, G. 1980, *MNRAS*, 193, 189
- Ferland, G. J., Korista, K. T., Verner, D. A., et al. 1998, *PASP*, 110, 761
- Furlong, M., Bower, R. G., Theuns, T., et al. 2015, *MNRAS*, 450, 4486
- Garrison-Kimmel, S., Boylan-Kolchin, M., Bullock, J. S., & Lee, K. 2014, *MNRAS*, 438, 2578
- Gill, S. P. D., Knebe, A., & Gibson, B. K. 2004, *MNRAS*, 351, 399
- Governato, F., Zolotov, A., Pontzen, A., et al. 2012, *MNRAS*, 422, 1231
- Guedes, J., Callegari, S., Madau, P., & Mayer, L. 2011, *ApJ*, 742, 76
- Guo, Q., White, S., Boylan-Kolchin, M., et al. 2011, *MNRAS*, 413, 101
- Hopkins, P. F., Kereš, D., Oñorbe, J., et al. 2014, *MNRAS*, 445, 581
- Hudson, M. J., Gillis, B. R., Coupon, J., et al. 2015, *MNRAS*, 447, 298
- Jonsson, P. 2006, *MNRAS*, 372, 2
- Kannan, R., Stinson, G. S., Macciò, A. V., et al. 2014, *MNRAS*, 437, 3529
- Keller, B. W., Wadsley, J., Benincasa, S. M., & Couchman, H. M. P. 2014, *MNRAS*, 442, 3013
- Knollmann, S. R., & Knebe, A. 2009, *ApJS*, 182, 608
- Kravtsov, A. V. 2013, *ApJL*, 764, LL31
- Kravtsov, A., Vikhlinin, A., & Meshcheryakov, A. 2014, *arXiv:1401.7329*
- Leauthaud, A., Tinker, J., Bundy, K., et al. 2012, *ApJ*, 744, 159
- Lupton, R., Blanton, M. R., Fekete, G., et al. 2004, *PASP*, 116, 133
- Mandelbaum, R., Seljak, U., Kauffmann, G., Hirata, C. M., & Brinkmann, J. 2006, *MNRAS*, 368, 715
- Marinacci, F., Pakmor, R., & Springel, V. 2014, *MNRAS*, 437, 1750
- Mo, H. J., Mao, S., & White, S. D. M. 1998, *MNRAS*, 295, 319
- More, S., van den Bosch, F. C., Cacciato, M., et al. 2011, *MNRAS*, 410, 210
- Moster, B. P., Somerville, R. S., Maulbetsch, C., et al. 2010, *ApJ*, 710, 903
- Moster, B. P., Naab, T., & White, S. D. M. 2013, *MNRAS*, 428, 3121
- Navarro, J. F., & Steinmetz, M. 2000, *ApJ*, 538, 477
- Noeske, K. G., Weiner, B. J., Faber, S. M., et al. 2007, *ApJL*, 660, L43
- Noordermeer, E., van der Hulst, J. M., Sancisi, R., Swaters, R. S., & van Albada, T. S. 2007, *MNRAS*, 376, 1513
- Oppenheimer, B. D., Davé, R., Kereš, D., et al. 2010, *MNRAS*, 406, 2325
- Penzo, C., Macciò, A. V., Casarini, L., Stinson, G. S., & Wadsley, J. 2014, *MNRAS*, 442, 176
- Piontek, F., & Steinmetz, M. 2011, *MNRAS*, 410, 2625
- Planck Collaboration, Ade, P. A. R., Aghanim, N., et al. 2014, *A&A*, 571, AA16
- Pontzen, A., Roškar, R., Stinson, G., & Woods, R. 2013, *Astrophysics Source Code Library*, 1305.002
- Price, D. J. 2008, *Journal of Computational Physics*, 227, 10040
- Reddick, R. M., Wechsler, R. H., Tinker, J. L., & Behroozi, P. S. 2013, *ApJ*, 771, 30
- Romeo Veloná, A. D., Sommer-Larsen, J., Napolitano, N. R., et al. 2013, *ApJ*, 770, 155
- Ritchie, B. W., & Thomas, P. A. 2001, *MNRAS*, 323, 743
- Saitoh, T. R., & Makino, J. 2009, *ApJL*, 697, L99
- Salim, S., Rich, R. M., Charlot, S., et al. 2007, *ApJS*, 173, 267
- Sawala, T., Frenk, C. S., Fattahi, A., et al. 2015, *MNRAS*, 448, 2941
- Schaye, J., Crain, R. A., Bower, R. G., et al. 2015, *MNRAS*, 446, 521
- Shen, S., Wadsley, J., & Stinson, G. 2010, *MNRAS*, 407, 1581

- Somerville, R. S., Hopkins, P. F., Cox, T. J., Robertson, B. E., & Hernquist, L. 2008, MNRAS, 391, 481
- Stark, D. P., Ellis, R. S., Bunker, A., et al. 2009, ApJ, 697, 1493
- Stinson, G., Seth, A., Katz, N., et al. 2006, MNRAS, 373, 1074
- Stinson, G. S., Brook, C., Macciò, A. V., et al. 2013, MNRAS, 428, 129
- Stinson, G. S., Dutton, A. A., Wang, L., et al. 2015, arXiv:1506.08785
- Somerville, R. S., & Davé, R. 2014, arXiv:1412.2712
- Tollet, E., Macciò, A. V., Dutton, A. A., et al. 2015, arXiv:1507.03590
- Vogelsberger, M., Genel, S., Springel, V., et al. 2014, MNRAS, 444, 1518
- Wadsley, J. W., Stadel, J., & Quinn, T. 2004, NewA, 9, 137
- Wadsley, J. W., Veeravalli, G., & Couchman, H. M. P. 2008, MNRAS, 387, 427
- Weinmann, S. M., Neistein, E., & Dekel, A. 2011, MNRAS, 417, 2737
- Weinmann, S. M., Pasquali, A., Oppenheimer, B. D., et al. 2012, MNRAS, 426, 2797
- White, S. D. M., & Rees, M. J. 1978, MNRAS, 183, 341
- White, S. D. M., & Frenk, C. S. 1991, ApJ, 379, 52
- Yang, X., Mo, H. J., & van den Bosch, F. C. 2003, MNRAS, 339, 1057
- Yang, X., Mo, H. J., van den Bosch, F. C., Zhang, Y., & Han, J. 2012, ApJ, 752, 41
- Yang, X., Mo, H. J., van den Bosch, F. C., Bonaca, A., Li, S., Lu, Y., Lu, Y., & Lu, X. 2013, ApJ, 770, 115

APPENDIX A: PARAMETERS

In this appendix we summarize all the galaxy and halo parameters for main target haloes at redshift $z = 0$ through this paper. Table A1 contains the simulation ID, the number of total particles, dark matter particles and star particles, virial mass, stellar mass and star formation rate.

Table A1. Galaxy and halo parameters for main target haloes at redshift $z = 0$

simulation ID	# particles n_{200}	# DM particles n_{DM}	# star particles n_{star}	virial mass (M_{200}/M_{\odot})	stellar mass (M_{star}/M_{\odot})	star formation rate ($M_{\odot} \text{ yr}^{-1}$)
g3.54e09	1,200,374	1,157,470	85	3.95×10^9	3.02×10^4	0.00
g4.36e09	1,278,589	1,167,760	79	9.54×10^9	3.30×10^4	0.00
g4.99e09	320,446	295,765	538	5.72×10^9	3.76×10^5	5.8×10^{-5}
g5.22e09	353,754	327,288	173	6.32×10^9	1.18×10^5	1.2×10^{-5}
g5.41e09	466,210	443,516	2,956	5.11×10^9	1.21×10^6	0.00
g5.59e09	358,332	335,527	2,520	6.46×10^9	1.74×10^6	1.7×10^{-4}
g5.84e09	555,955	512,178	87	5.95×10^9	1.16×10^5	6.3×10^{-5}
g7.05e09	584,878	544,306	3,249	1.05×10^{10}	2.27×10^6	0.00
g7.34e09	559,724	521,731	331	6.05×10^9	4.22×10^5	0.00
g9.26e09	581,361	527,275	132	6.14×10^9	5.37×10^4	0.00
g1.09e10	690,285	546,318	9,204	1.09×10^{10}	6.55×10^6	0.00
g1.18e10	628,317	565,451	4,944	1.10×10^{10}	3.41×10^6	0.00
g1.23e10	515,485	468,423	2,314	9.08×10^9	1.60×10^6	0.00
g1.44e10	1,159,093	834,135	9,656	1.70×10^{10}	6.69×10^6	0.00
g1.47e10	862,592	784,867	13,043	1.52×10^{10}	9.00×10^6	1.3×10^{-3}
g1.50e10	791,452	725,701	5,055	1.40×10^{10}	3.42×10^6	0.00
g1.57e10	728,314	670,688	13,027	1.29×10^{10}	8.93×10^6	0.00
g1.88e10	1,063,823	971,852	23,864	1.88×10^{10}	1.65×10^7	3.9×10^{-3}
g1.89e10	1,401,592	1,060,626	17,813	2.13×10^{10}	1.29×10^7	3.1×10^{-3}
g1.90e10	1,457,806	1,222,038	17,279	2.40×10^{10}	1.20×10^7	1.4×10^{-3}
g1.92e10	1,272,888	990,462	8,255	1.98×10^{10}	5.30×10^6	1.4×10^{-4}
g1.95e10	794,621	704,686	5,488	1.37×10^{10}	3.82×10^6	0.00
g2.09e10	1,018,898	839,068	13,600	1.66×10^{10}	9.35×10^6	0.00
g2.34e10	1,500,299	1,319,369	19,729	2.57×10^{10}	1.36×10^7	0.00
g2.37e10	1,503,953	1,232,912	25,627	2.43×10^{10}	9.65×10^6	0.00
g2.39e10	869,294	743,922	8,601	1.46×10^{10}	5.94×10^6	1.7×10^{-4}
g2.63e10	458,723	414,291	18,388	2.70×10^{10}	4.28×10^7	0.00
g2.64e10	2,340,543	1,579,110	43,275	3.26×10^{10}	2.93×10^7	0.00
g2.80e10	521,957	413,400	15,628	2.77×10^{10}	3.68×10^7	2.5×10^{-3}
g2.83e10	483,150	370,911	13,428	2.50×10^{10}	2.96×10^7	0.00
g2.94e10	1,908,993	1,657,184	85,637	3.22×10^{10}	5.86×10^7	4.2×10^{-4}
g3.19e10	677,287	525,030	10,679	3.54×10^{10}	1.47×10^7	3.9×10^{-5}
g3.44e10	1,077,981	694,131	26,561	4.88×10^{10}	6.32×10^7	4.7×10^{-3}
g3.67e10	547,857	480,668	23,584	3.15×10^{10}	5.49×10^7	0.00
g3.93e10	682,659	477,948	16,007	3.30×10^{10}	3.75×10^7	0.00
g4.27e10	885,293	616,773	26,191	4.25×10^{10}	6.16×10^7	4.4×10^{-3}
g4.48e10	1,191,821	895,736	58,334	6.04×10^{10}	1.37×10^8	3.9×10^{-5}
g4.86e10	1,051,559	757,795	52,672	5.16×10^{10}	1.22×10^8	3.7×10^{-3}
g4.94e10	984,362	791,322	48,035	5.26×10^{10}	1.11×10^8	7.8×10^{-3}
g4.99e10	940,085	732,808	52,511	4.90×10^{10}	1.22×10^8	9.4×10^{-3}
g5.05e10	777,412	650,173	40,840	4.29×10^{10}	9.47×10^7	7.8×10^{-5}
g6.12e10	986,798	733,881	39,024	4.97×10^{10}	9.13×10^7	7.8×10^{-5}
g6.37e10	2,621,929	1,617,864	95,020	1.15×10^{11}	2.12×10^8	1.2×10^{-2}
g6.77e10	2,118,102	1,333,784	204,017	9.28×10^{10}	4.84×10^8	8.7×10^{-2}
g6.91e10	1,331,679	1,069,321	107,120	7.08×10^{10}	2.50×10^8	2.9×10^{-3}
g7.12e10	1,009,755	715,315	58,766	4.88×10^{10}	1.37×10^8	1.5×10^{-2}
g8.89e10	591,924	397,347	50,174	9.22×10^{10}	4.02×10^8	2.9×10^{-2}
g9.59e10	614,423	368,306	34,468	8.84×10^{10}	2.76×10^8	8.7×10^{-2}
g1.05e11	775,657	505,507	70,478	1.18×10^{11}	5.67×10^8	6.0×10^{-2}
g1.08e11	785,537	520,108	108,025	1.20×10^{11}	8.47×10^8	2.7×10^{-2}
g1.37e11	1,014,522	653,073	252,530	1.48×10^{11}	2.02×10^9	9.5×10^{-2}
g1.52e11	1,128,519	657,385	112,285	1.57×10^{11}	7.92×10^8	3.8×10^{-2}
g1.57e11	1,076,183	677,124	143,921	1.58×10^{11}	1.15×10^9	6.7×10^{-2}
g1.59e11	1,223,754	691,453	86,944	1.68×10^{11}	6.69×10^8	7.9×10^{-4}
g1.64e11	1,468,563	786,245	111,008	1.93×10^{11}	9.13×10^8	0.38
g2.04e11	1,722,119	901,588	573,355	2.09×10^{11}	4.70×10^9	0.79
g2.19e11	920,447	557,247	113,958	1.31×10^{11}	9.27×10^8	9.8×10^{-2}
g2.39e11	2,133,166	1,109,605	698,696	2.58×10^{11}	5.80×10^9	1.12
g2.41e11	1,939,348	1,092,825	501,991	2.53×10^{11}	4.10×10^9	0.62
g2.42e11	2,073,620	1,175,947	689,091	2.68×10^{11}	5.48×10^9	0.39
g2.54e11	2,004,595	1,144,673	424,390	2.67×10^{11}	3.50×10^9	0.87

Table A2. cont'd Galaxy and halo parameters for main target haloes at redshift $z = 0$

simulation ID	# particles n_{200}	# DM particles n_{DM}	# star particles n_{star}	virial mass (M_{200}/M_{\odot})	stellar mass (M_{star}/M_{\odot})	star formation rate ($M_{\odot} \text{ yr}^{-1}$)
g3.06e11	2,688,990	1,323,580	906,552	3.11×10^{11}	7.42×10^9	1.25
g3.21e11	2,342,924	1,272,210	448,644	3.03×10^{11}	3.67×10^9	1.10
g3.23e11	631,510	371,614	44,745	8.93×10^{10}	3.60×10^8	5.5×10^{-2}
g3.49e11	3,276,200	1,815,975	539,486	4.33×10^{11}	3.97×10^9	0.61
g3.55e11	3,241,957	1,760,597	480,380	4.23×10^{11}	3.85×10^9	0.66
g3.59e11	2,762,536	1,459,228	534,349	3.49×10^{11}	4.36×10^9	0.74
g3.71e11	4,015,748	1,691,651	1,535,547	4.08×10^{11}	1.24×10^{10}	1.49
g4.90e11	2,452,320	1,369,494	428,202	3.25×10^{11}	3.43×10^9	0.42
g5.02e11	5,258,849	2,408,247	1,821,403	5.75×10^{11}	1.46×10^{10}	0.92
g5.31e11	3,534,992	2,204,411	559,381	5.28×10^{11}	1.64×10^{10}	2.26
g5.36e11	4,505,028	2,889,033	445,661	6.88×10^{11}	1.18×10^{10}	3.88
g5.38e11	4,187,358	2,726,961	648,971	6.46×10^{11}	1.85×10^{10}	1.24
g5.46e11	2,459,236	1,374,445	470,795	3.25×10^{11}	3.78×10^9	0.37
g5.55e11	5,020,346	2,200,598	2,075,884	5.20×10^{11}	1.71×10^{10}	2.75
g6.96e11	1,094,722	412,962	498,881	8.00×10^{11}	3.30×10^{10}	10.40
g7.08e11	1,098,831	412,287	479,668	8.06×10^{11}	3.05×10^{10}	3.66
g7.44e11	1,294,128	596,875	283,637	1.18×10^{12}	1.85×10^{10}	12.95
g7.55e11	1,185,149	455,930	483,752	8.93×10^{11}	3.11×10^{10}	2.92
g7.66e11	1,528,867	478,007	911,988	9.30×10^{11}	5.92×10^{10}	2.71
g8.06e11	1,366,038	481,349	665,796	9.43×10^{11}	4.48×10^{10}	13.19
g8.13e11	1,704,130	505,171	1,043,618	9.91×10^{11}	6.68×10^{10}	3.67
g8.26e11	1,513,265	518,236	739,749	1.02×10^{12}	4.68×10^{10}	2.04
g8.28e11	1,276,937	591,330	275,702	1.16×10^{12}	1.77×10^{10}	1.01
g1.12e12	1,977,112	564,785	1,222,359	1.12×10^{12}	7.85×10^{10}	4.29
g1.77e12	3,668,318	1,117,439	2,173,715	2.19×10^{12}	1.39×10^{11}	8.47
g1.92e12	4,018,048	1,200,667	2,467,821	2.34×10^{12}	1.58×10^{11}	8.13
g2.79e12	5,598,386	1,800,095	3,099,962	3.53×10^{12}	1.96×10^{11}	11.09